Chaos in Spin-Wave Instabilities

——*Theory and Experiments*——

Hitoshi YAMAZAKI and Michinobu MINO

Department of Physics, Okayama University, Okayama 700

(Received February 25, 1989)

Parametric excitation of spin-waves with high microwave power causes spin-wave instability where number of spin-waves grows exponentially with time beyond thermal level. Above the spin-wave instability threshold, auto-oscillations of magnon number which include cascade of period-doubling bifurcations, chaos, periodic window and period-halving have been experimentally observed. From experimental time-series data, return maps, fractal dimensions, positive Lyapunov exponents, phase space portraits of strange attractors and two-dimensional Poincaré sections are obtained. A theoretical model of chaos due to nonlinear four-magnon interaction under parallel pumping is given. Numerical solutions display a rich variety of periodic and chaotic trajectories. A multi-fractal structure, singularity spectrum $f(\alpha)$, is numerically studied for two modes model which includes a microwave cavity mode.

Contents

§ 1. Introduction

Ferromagnetic resonance (abbreviated to FMR) was discovered in 1946, that is shortly after the discovery of paramagnetic and nuclear magnetic resonance. Since then FMR is well known as a very important method to study ferromagnetic materials. Investigation of the uniform mode makes it possible to derive the g-factor and

various anisotropy coefficients from experimental results of the resonance frequency or resonance field. FMR in a thin film is known as spin-wave resonance from which exchange constants are derived. Behavior of magnetic resonance absorption under high radiation field is important to study magnetic relaxation which includes the spin-spin and spin-lattice interactions. According to the Bloch-Bloembergen equation, which is originally derived for paramagnetic resonance, the transfer of energy from the spin system to the lattice is described by the spin-lattice relaxation time, T_1. The spin-spin relaxation time T_2 is estimated by linewidth. High-power behavior of resonance absorption is commonly applied to study these two relaxation times, T_1 and T_2. Accordingly the saturation effect in the ferromagnetic resonance absorption has been measured by many researchers to study relaxation phenomena in ferromagnetic material.

Damon[1] and Bloembergen and Wang[2] have performed FMR experiment at high microwave power levels and found two anomalous effects which could not be explained by the conventional theory of paramagnetic relaxation. These effects are as follows: (1) Saturation of the intensity of FMR line begins at a power level far below that for saturation of the longitudinal component of the magnetization. (2) A subsidiary broad absorption appears at applied field lower than the main resonance line. The theoretical explanation to these two phenomena has been given by Suhl[3] and is referred to as the Suhl instability or the spin-wave instability. His theory is the opening of a new field of nonlinear spin dynamics. These phenomena are explained as the nonlinear generation of $\boldsymbol{k}\neq 0$ magnons by the uniform mode ($\boldsymbol{k}=0$ magnon). The subsidiary absorption results from the generation of a pair of magnons with the wave vectors $\boldsymbol{k}$ and $-\boldsymbol{k}$ from a uniform mode. .This is a three-magnon process and is referred to as the first-order Suhl instability. The saturation of the main resonance is due to the generation of a pair of magnons $\boldsymbol{k}$ and $-\boldsymbol{k}$ from a pair of $\boldsymbol{k}=0$ magnons. This four-magnon process is referred to as the second-order Suhl instability. Suhl represented these phenomena as follows: The power transfer becomes catastrophic above a certain threshold power levels. The spin-waves grow with time exponentially to a large nonthermal value. This situation bears a certain resemblance to the turbulent state in fluid dynamics. Recently interest in chaotic phenomena is indeed growing in the field of nonlinear spin dynamics.

Parallel pumping, which was initiated by Schlömann, Green and Milano[4] and Morgenthaler,[5] is a more powerful technique than perpendicular one denoted above, because it is possible to generate spin-wave instability of individual spin-waves with definite wave vectors. In parallel-pumping experiment, as the name denotes, a microwave magnetic field is applied parallel to the static magnetic field. As the microwave magnetic field is increased beyond some critical value, the number of magnons in a very narrow region in wave number space grows exponentially, while the others stay almost at the thermal equilibrium level. These magnons have half the pumping frequency and equal and opposite wave vectors whose magnitude can be selected by varying the static magnetic field. The amplitude of these magnons is limited by a balance between the strength of the driving power and magnon damping. Since the grown magnons constitute standing waves, the dynamical transverse component of the magnetizations is considered to be in an ordered state. By increasing the

driving power further, this nonequilibrium stationary state is occasionally broken by occurrence of oscillations of magnon amplitude. Nonperiodic auto-oscillations of magnon amplitudes under parametric excitation has been known since the early stage of these kinds of experiments.[6)~9)] Hartwick et al.[6)] have first observed auto-oscillations under both parallel and perpendicular pumping in an yttrium iron garnet (YIG). Those were generally called relaxation oscillations. Zautkin and Starobinets[8)] have extensively studied the oscillations in YIG. They measured threshold microwave power for the oscillations and dependence of the oscillation frequencies on temperature and the magnetic field. They explained that the phenomena above the threshold for spin-wave instability were governed by nonlinear spin dynamics.

Zakharov, L'vov and Starobinets[10),11)] have theoretically showed that spin-wave turbulence could occur by nonlinear magnon-magnon interactions. They have found nonperiodic oscillations of magnon amplitude under strong parametric excitation by numerically solving four-magnon interaction Hamiltonian which they called S theory. Further development of irregular oscillations was carried out by Nakamura and co-workers.[12),13)] They examined numerically a nonlinear dynamical equation of parametrically excited magnon pairs (four-magnon process) which was introduced by Zakharov et al.[10),11)] Oscillations of limit cycle behavior change to show the subharmonics of the fundamental frequency above a certain driving power. Following a cascade of period-doubling bifurcations, they found chaotic behavior of the driven ferromagnet. It is now well known that successive period-doubling bifurcations are typical routes to chaos.[14)] These theoretical studies have stimulated the experimental search for chaotic dynamics in spin-wave instabilities. Similar phenomena in the perpendicular pumping case have been theoretically studied by Zhang and Suhl[15)] and Rezende et al.[16)] Period-doubling bifurcations of magnon oscillations under parallel pumping in the antiferromagnet $CuCl_2 2H_2O$ were observed by Yamazaki.[17)] Jeffries and co-workers[18)~23)] studied intensively chaotic phenomena of magnons for high-power ferromagnetic resonance in YIG. Carroll et al.[23)] and Benner et al.[24)] have also studied chaos of the first-order Suhl instability in YIG. Rezende and co-workers[25),26)] observed period-doubling and chaos in parallel-pumped magnons in YIG. Characterization of chaos and strange attractors of parallel-pumped magnons in YIG and $(CH_3NH_3)_2CuCl_4$ (abbreviated to MACC) has been studied by the present authors and co-workers.[27)~31)] Smirnov[32)] observed chaotic oscillations in antiferromagnetic $CsMnF_3$. Waldner and co-workers[33)~35)] studied oscillations of irregular periods in antiferromagnetic crystals and developed a stroboscopic model by a classical torque equation.

Unstable growth of spin-waves is possible under parametric excitation when spin-wave mode is weakly damped and comparatively isolated. Let us survey nonequilibrium phase transitions in the driven magnon system. The number of magnons under parallel pumping is schematically shown in Fig. 1 as a function of driving microwave power. By increasing the driving power further beyond the instability threshold, the nonequilibrium stationary state is occasionally broken by the occurrence of oscillations of magnon amplitudes. The possible mechanism of the oscillations is as follows. The oscillations may occur by the existence of a nonlinear interaction between the driven magnon mode (we call it a $\boldsymbol{k}$-magnon) and another

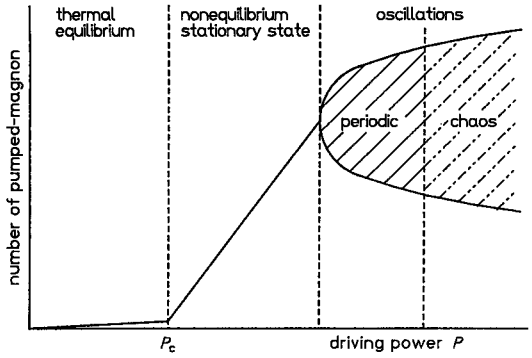

Fig. 1. Number of parallel-pumped magnons is schematically shown as a function of driving microwave power.

magnon mode ($\boldsymbol{k}'$-magnon). When the $\boldsymbol{k}$-magnon increases far beyond the thermal equilibrium level, $\boldsymbol{k}'$-magnons begin to increase by getting energy through the $\boldsymbol{k}$-magnon mode. If the number of $\boldsymbol{k}'$-magnons increases above some critical value, they exceed the thermal equilibrium value. As a consequence of reaction, $\boldsymbol{k}'$-magnons excite the $\boldsymbol{k}$-magnon, but the phase of this reaction field is retarded relative to the external driving field because of relaxation of the $\boldsymbol{k}'$-magnons. This time-delayed feedback causes auto-oscillations of magnon number. The frequency of this oscillation is determined by magnon relaxation and is usually much smaller than the precession frequency. The regular oscillations become chaotic through cascade of period-doubling bifurcations. This phase transition scheme bears resemblance to that of other nonequilibrium dissipative systems; for example, Rayleigh-Benard convection.[36] That is to say, the thermal equilibrium state, standing-waves, oscillations and chaos of magnon amplitudes correspond to thermal convection, convection rolls, oscillation of rolls and turbulence in the convection system, respectively.

§ 2. Theory of spin-wave instability

2.1. *Parallel pumping*

Parallel-pumping experiment is performed in a way that the microwave magnetic field is applied parallel to the static magnetic field. Precession paths of spins are generally elliptical due to the magnetic dipolar and other anisotropies. Therefore the longitudinal component of the magnetization oscillates at twice the frequency of the transverse components. The oscillating longitudinal component of a standing wave, a pair of traveling-wave magnons with equal and opposite wave vectors, can interact with the uniform microwave magnetic field. Since the number of magnons which interact with the pumping field is very small with the thermal level, absorption intensity is normally very small. However as the pumping power is increased beyond a certain critical value, power absorbed by a sample comes to be measurable because of exponential growth of $\boldsymbol{k}$ and $-\boldsymbol{k}$ magnon pairs.

The Hamiltonian we consider consists of the exchange, the dipolar, the Zeeman terms, and is written as

$$H=H_{\mathrm{ex}}+H_{\mathrm{dip}}+H_{\mathrm{z}}\,, \tag{1}$$

$$H_{\mathrm{ex}}=-2J\sum_{\langle lm\rangle}\boldsymbol{S}_l\boldsymbol{S}_m\,, \tag{2}$$

$$H_{\mathrm{dip}}=\sum_{l>m}\frac{(g\mu_{\mathrm{B}})^2}{r_{lm}^5}\{r_{lm}^2(\boldsymbol{S}_l\boldsymbol{S}_m)-3(\boldsymbol{r}_{lm}\boldsymbol{S}_l)(\boldsymbol{r}_{lm}\boldsymbol{S}_m)\}\,, \tag{3}$$

$$H_Z=-g\mu_{\mathrm{B}}H_0\sum_l S_{lz}\,, \tag{4}$$

where the magnetic field $\boldsymbol{H}_0$ is directed along the z-axis. The following Hamiltonian is obtained by using magnon-creation and annihilation operators,

$$H=E_0+\sum_k\left\{A_k a_k^{+}a_k+\frac{1}{2}(B_k a_k a_{-k}+B_k^{*}a_k^{+}a_{-k}^{+})\right\}, \tag{5}$$

$$A_k=2zJS(1-\gamma_k)+g\mu_{\mathrm{B}}H_0+S\sum_{r_{lm}\neq 0}\frac{3z_{lm}^2-r_{lm}^2}{r_{lm}^5}\left(1+\frac{1}{2}e^{ikr_{lm}}\right), \tag{6}$$

$$B_k=-\frac{3}{2}S\sum_{r_{lm}\neq 0}\frac{x_{lm}^2-y_{lm}^2-2ix_{lm}y_{lm}}{r_{lm}^5}e^{ikr_{lm}}\,. \tag{7}$$

Because of the dipolar interaction the a_k is not the normal mode. Hamiltonian is transformed in terms of normal mode c_k as follows,

$$H=E_0+\sum_k\varepsilon_k\left(c_k^{+}c_k+\frac{1}{2}\right)-\frac{1}{2}\sum_k A_k\,. \tag{8}$$

The spin-wave energy is given by

$$\varepsilon_k=(A_k^2-|B_k|^2)^{1/2}\,. \tag{9}$$

Parallel pumping by a microwave magnetic field $H_1\cos(\omega_{\mathrm{p}}t)$ is given by the following perturbation Hamiltonian,

$$\begin{aligned}H_1&=-g\mu_{\mathrm{B}}H_1\cos(\omega_{\mathrm{p}}t)\sum_l S_{lz}\\&=\gamma H_1\cos(\omega_{\mathrm{p}}t)\sum_k\frac{|B_k|}{2\hbar w_k}(c_k^{+}c_{-k}^{+}+\mathrm{c.c.})\,,\end{aligned} \tag{10}$$

where $\hbar\omega_k$ is the spin-wave energy, $\gamma\hbar=g\mu_{\mathrm{B}}$ and H_1 the amplitude of microwave magnetic field of the frequency ω_{p}. This term corresponds to the creation of $\boldsymbol{k}$ and $-\boldsymbol{k}$ magnon pairs.

The growth rate of the particular magnon pair is

$$\frac{dn_k}{dt}=\pi\hbar\gamma^2H_1^2\frac{|B_k|^2}{(\hbar\omega_k)^2}n_k\delta(\omega_{\mathrm{p}}-2\omega_k)\,. \tag{11}$$

If the final two-magnon state has the finite relaxation rate, which is conventionally written as $\gamma(\Delta H_k)$, the delta function is to be replaced by

$$\delta(\omega_{\mathrm{p}}-2\omega_k)\rightarrow\frac{\gamma(\Delta H_k)}{\pi\hbar[(\omega_{\mathrm{p}}-2\omega_k)^2+\gamma^2(\Delta H_k)^2]} \tag{12}$$

The decay rate of the pumped magnon is phenomenologically introduced as follows,

$$\frac{dn_k}{dt}=-\gamma(\Delta H_k)n_k\,, \tag{13}$$

where ΔH_k is the spin-wave linewidth. When the growth rate exceeds the decay rate, spin-wave instability occurs. A threshold is given by

$$\pi\hbar\gamma^2 H_1^2 \frac{|B_k|^2}{(\hbar\omega_k)^2} = -\gamma(\Delta H_k) . \tag{14}$$

By microwave driving above the threshold, the particular magnon, which has the minimum threshold, grows with time exponentially to a large nonthermal value, while the others stay almost at the thermal equilibrium levels.

2.2. *Suhl instability*

Suhl[3] has first developed the theory of spin-wave instability by perpendicular pumping and derived a threshold microwave magnetic field. The three- and four-magnon processes give rise to the first- and second-order Suhl instability at high power levels. The dipolar Hamiltonian contains terms which are of third order in magnon creation and annihilation operators.

The first step of the process is the excitation of the uniform mode ($\boldsymbol{k}=0$ mode) by the microwave magnetic field. In the next step, energy is fed from the $\boldsymbol{k}=0$ mode to the other mode by a splitting process. Some particular pair of spin-waves $\boldsymbol{k}$ and $-\boldsymbol{k}$, which is most strongly coupled to the uniform mode, grows exponentially when the rate of energy fed into them via the $\boldsymbol{k}=0$ mode exceeds the rate at which they are able to lose energy. We consider the following Hamiltonian which represents the three-magnon splitting process,

$$H_{0\to k,-k} = \sum_k [B(k,-k) a_0 a_k^+ a_{-k}^+ + B^*(k,-k) a_0^+ a_k a_{-k}] . \tag{15}$$

If $n_0 \gg n_k \gg 1$, where n_k is the number of the $\boldsymbol{k}$-magnon, the growth rate of n_k via the uniform-mode magnons is given by

$$\frac{dn_k}{dt} = \frac{16\pi}{\hbar} |B(k,-k)|^2 n_0 n_k \delta(\omega_f - \omega_i) . \tag{16}$$

When the energy conservation is satisfied in the splitting process, the total rate equation of the number of $\boldsymbol{k}$ and $-\boldsymbol{k}$ magnon pair is consequently given by

$$\frac{dn_k}{dt} = \frac{16}{\hbar^2} |B(k,-k)|^2 \frac{n_0 n_k}{\gamma(\Delta H_k)} - \gamma(\Delta H_k) n_k . \tag{17}$$

The first-order spin-wave instability occurs when the growth rate exceeds the decay rate, that is, $dn_k/dt \geqq 0$. The second-order Suhl instability, which arises from the four-magnon scattering process, is derived with a similar procedure.

§ 3. Theory of chaos in parallel-pumped magnons

In this section chaotic characteristics of magnon system under parallel pumping will be theoretically described.[20),22),37)] Numerical calculation of a nonlinear dynamical equation of parametrically excited magnon pairs gives a cascade of period-doubling bifurcations and chaotic oscillations. It is found to show rich structures of chaos and turbulence comparable to those in fluid dynamics. A multi-fractal struc-

ture of Poincaré sections will be examined by increasing a driving power.

We consider a magnon system under parallel pumping with four-magnon interaction which includes the effect of a microwave cavity mode. The Hamiltonian with $\hbar=1$ is given as follows,

$$H=\omega_p A^+A+\sum_k \omega_k b_k^+ b_k+\frac{1}{2}\sum_k (g_k A b_k^+ b_{-k}^+ +\text{h.c.})$$
$$+(h_p V\exp(-i\omega_p t)A^+ +\text{h.c.})+H_{\text{int}}, \tag{18}$$

$$H_{\text{int}}=\sum_{kk'}\left(T_{kk'} b_k^+ b_k b_{k'}^+ b_{k'}+\frac{1}{2}S_{kk'} b_k b_{-k} b_{k'}^+ b_{-k'}^+\right), \tag{19}$$

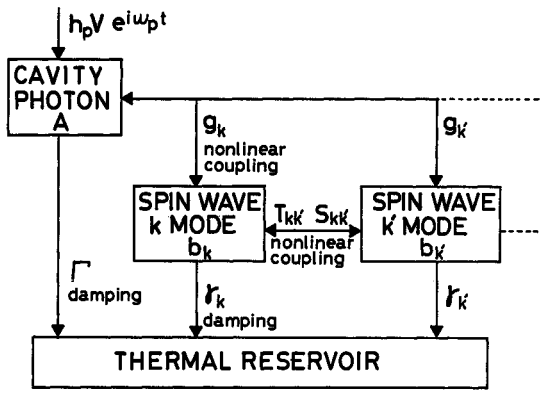

Fig. 2. Schematic diagram of the model Hamiltonian; Eqs. (18) and (19).

where ω_p the pumping frequency, ω_k the magnon frequency, A^+ and A the creation and annihilation operators of photons in the microwave cavity, b_k^+ and b_k the creation and annihilation operators of magnons, g_k the nonlinear coupling parameters between photons and magnons, T and S the nonlinear coupling parameters due to the four-magnon interaction. The model is schematically shown in Fig. 2. The equations of motion with phenomenological damping terms are given as follows,

$$\frac{dA}{dt}+\Gamma A=-i\frac{\partial H}{\partial A^+}, \tag{20}$$

$$\frac{db_k}{dt}+\gamma_k b_k=-i\frac{\partial H}{\partial b_k^+}. \tag{21}$$

Here we introduce slow variables,

$$A=\tilde{A}\exp(-i\omega_p t), \tag{22}$$

$$b_k=c_k\exp(-i\omega_p t/2). \tag{23}$$

If a cavity is very dissipative, $\tilde{A}$ follows c_k adiabatically and can be eliminated. Therefore the equation of motion for spin-wave modes $c_k(=c_{-k})$ become as follows,

$$\frac{dc_k}{dt}=-\gamma_k c_k-i\Delta\Omega_k c_k-iQFg_k c_k^*$$
$$-i\{2\sum_{k'}T_{kk'}|c_{k'}|^2 c_k+\sum_{k'}(S_{kk'}+Eg_k g_{k'}^*)c_{k'}^2 c_k^*\}, \tag{24}$$

where γ_k, $\Delta\Omega_k$ and F are the damping constants for c_k, frequency shift $\omega_k-\omega_p/2$ and a driving field $(=h_p V)$, respectively. Q and E are given as $-i/\Gamma$ and $-i/(2\Gamma)$, respectively with use of the damping constant Γ for the cavity mode. The coupling constant g_k between the cavity mode and magnon mode c_k vanishes for the mode

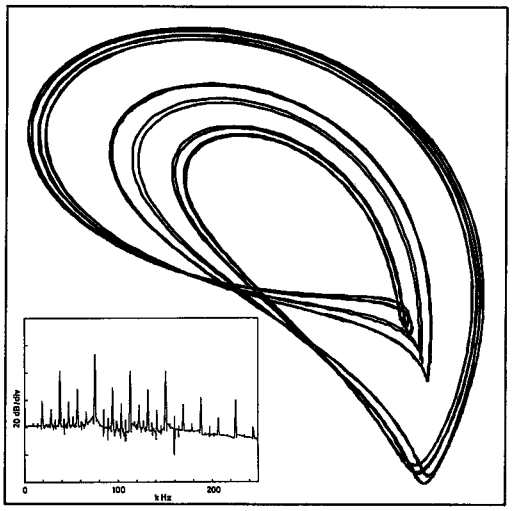

Fig. 3. Projection of a strange attractor on the $\mathrm{Re}C_1$-$\mathrm{Im}C_1$ plane at $F=F_c=1.92286$. (Inset is a power spectrum.)[37]

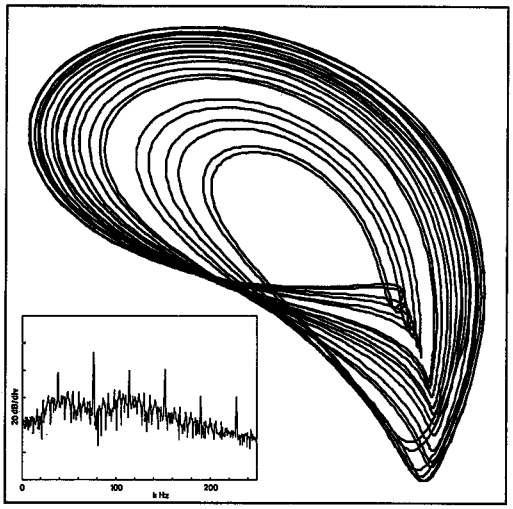

Fig. 4. Projection of a strange attractor on the $\mathrm{Re}C_1$-$\mathrm{Im}C_1$ plane at $F=F_c=1.94$. (Inset is a power spectrum.)[37]

propagating parallel to a static field. We now confine to the case of two modes system where $g_{k1}\neq 0$ and $g_{k2}=0$. For simplicity we take F instead of $F\times 10^7$ in the following description.

Numerical solutions of Eq. (24) obtained by Runge-Kutta methods display a rich variety of periodic and chaotic trajectories depending on the intensity of driving field. Ohta and Nakamura[13] found a cascade of period-doubling bifurcations with scaling constant of $\delta=4.675$ which is in good agreement with the Feigenbaum universal constant, 4.6692.[14] The period-doubling bifurcations accumulate at the critical point, $F=F_c=1.92286$. The strange attractor and power spectrum at $F=F_c$ are shown in Fig. 3. With increasing F, the strange attractor gradually grows to a higher dimensional one as shown in Fig. 4.

Halsey et al.[38] have developed a singularity spectrum $f(\alpha)$ to describe the global structure of an attractor. We proceed to calculate $f(\alpha)$ by using the Poincaré section which is divided into very small blobs. A partition function is given as follows,

$$\Gamma(q,l)=\langle p_i(l)^{q-1}\rangle\,, \tag{25}$$

where the probability $p_i(l)$ is obtained by counting the number of points within the i-th blob with radius l and dividing by the total number of points in the Poincaré section data set. The brackets represent an average over all the blobs. For small l, behavior of $\Gamma(q,\ l)$ is expected as

$$\Gamma(q,l)\sim l^{\tau(q)}\,. \tag{26}$$

The $f(\alpha)$ spectrum is obtained from $\tau(q)$ with the use of the Legendre transformation,

$$\alpha(q)=d\tau(q)/dq\,, \tag{27}$$

$$f(q)=q\alpha-\tau(q)\,. \tag{28}$$

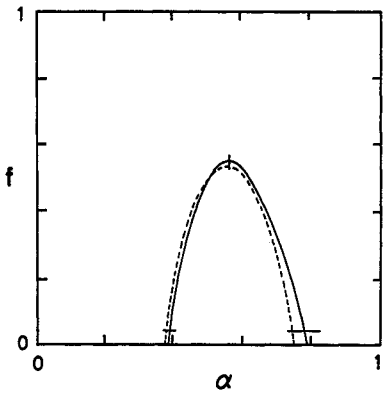

Fig. 5. The $f(\alpha)$ spectrum at $F=F_c$.[37] Broken line is a universal curve.[38]

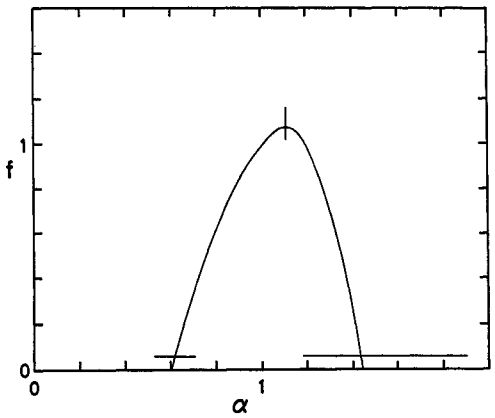

Fig. 6. The $f(\alpha)$ spectrum at $F=1.94$.[37]

The curve $f(\alpha)$ at $F=F_c$ is found to be in good agreement with the universal one due to a logistic model[38] as shown in Fig. 5. Figure 6 shows the $f(\alpha)$ at $F=1.94$ which has a larger fractal dimension $D_0=1.07$.

§ 4. Experimental observation of chaos under parallel pumping

4.1. *Samples*

Experimental data shown below are obtained from an yttrium iron garnet ($Y_3Fe_5O_{12}$; YIG) and methylammonia tetrachlorocuprate ($(CH_3NH_3)_2CuCl_4$; MACC). YIG is a cubic insulating ferrimagnet with a Curie temperature of 559 K. The net magnetization is due to the resultant of two oppositely magnetized sublattices of Fe^{3+} ions. The Fe^{3+} ions have a ($S=5/2$, $L=0$) ground state, and consequently a weak interaction with the crystal lattice. MACC is a two-dimensional ferromagnet below $T_c=8.9$ K. The crystal structure is face-centered monoclinic which consists of ferromagnetic layers (the c-plane) coupled by a very weak ferromagnetic interaction; the ratio of the interlayer exchange interaction to the intralayer one is 7.9×10^{-5}. Cu^{2+} ions have a spin $S=1/2$ with isotropic g-value 2.167 within the c-plane.

4.2. *Experimental procedure*

Parallel-pumping experiments were made at a pumping frequency of 9 GHz band at liquid-helium temperatures. Both the static and microwave magnetic fields are applied along the spin-easy axis [111] for YIG and along the b-axis for MACC. The microwave apparatus is a standard reflection-type setup. Microwave signals reflected from the sample cavity of a TE_{101} mode are detected by a diode and recorded in a computer file as a function of time.

4.3. *Auto-oscillations and power spectra*

Experiments were performed at a pumping frequency of 8.86 GHz at a tempera-

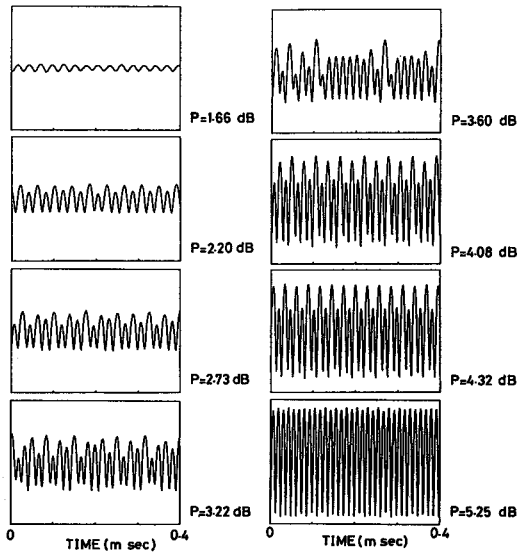

Fig. 7. Observed oscillation signals at various microwave power in YIG.[27] The threshold for spin-wave instability is taken as $P=0$ dB.

ture of 4.2 K. A disk-shaped YIG, 1.28 mm in diameter and 0.40 mm thick is mounted on the bottom of the cavity. Both the microwave and the static magnetic fields are applied along the [111] direction which is perpendicular to the disk. The measurements were done in a field of 1935G where the minimum threshold, $P_c=0.3$ mW, occurs. In this field, magnons propagating perpendicular to the static field and having the wave number of $\boldsymbol{k}\sim 0$ are excited.

Figure 7 shows a part of real-time absorption signals at various power levels. The driving microwave power P is normalized by the threshold for spin-wave instability. By increasing the driving power, periodic, period-2 and aperiodic oscillations are observed. Figure 8 shows power spectra of the oscillations of Fig. 7. By increasing the driving power, a fundamental frequency f_0 increases significantly as shown in Fig. 9. As the power is increased to $P=2.20$ dB, a sharp subharmonic component appears at $f_0/2=24.4$ kHz. This component becomes a broad band without showing a clear $f_0/4$ component. At $P=3.22$ and 3.60 dB the oscillations are aperiodic and thus the corresponding power spectra exhibit broad bands. By increasing the power further, the oscillations become periodic again and exhibit period-halving; reverse of period-

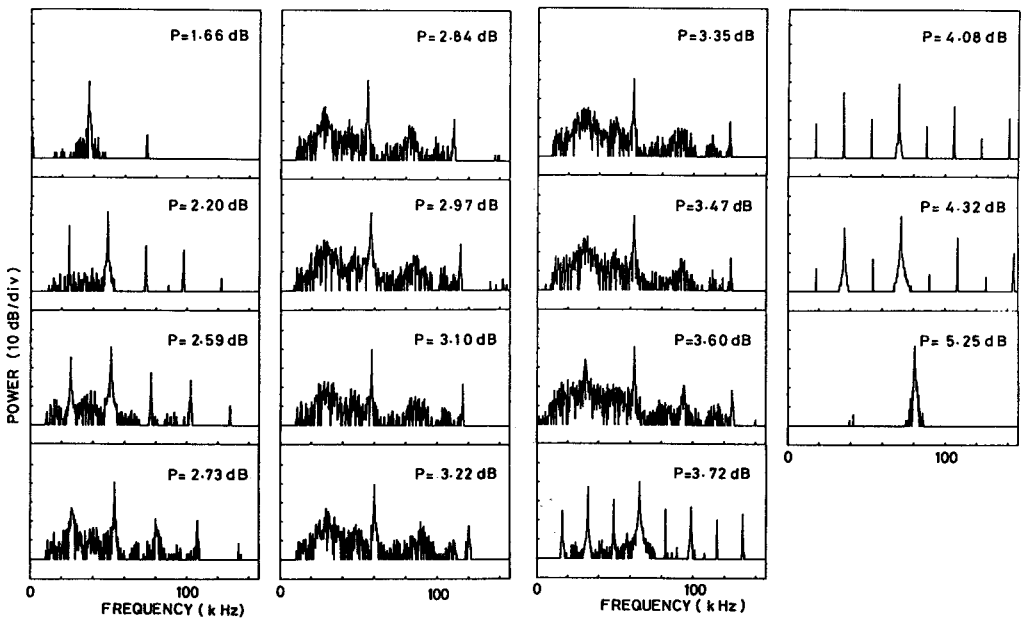

Fig. 8. Power spectra at various microwave power in YIG.[27]

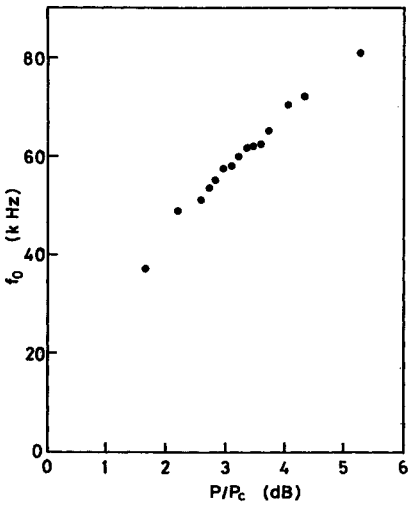

Fig. 9. Power dependence of fundamental frequency in YIG.

doubling, i.e., period-4, period-2 and period-1. The fundamental frequency and the peak-to-peak amplitude keep to increase with increasing the power. Period-4, period-2 and period-1 are observed at $P=4.08$, 4.32 and 5.25 dB, respectively and have $f_0=70.3$, 72.0 and 80.6 kHz, respectively.

4.4. *Strange attractors*

In order to understand a dynamical system, it is useful to know trajectories in the multidimensional phase space. An instantaneous state of the dynamical system is described by a point which moves along a curve, a phase-space trajectory, as time varies. The observed data in the experiment are single time series data of the number of parallel-pumped magnons. Those magnons interact with other specific magnon modes and this interaction causes auto-oscillations. Multidimensional trajectories are constructed by the time series data of several magnon modes. However, we have no way to separately measure the number of different magnon modes at this moment. The conventional method to generate multidimensional data from the original single time series data is a procedure of time delay.[39),40)] For example, three-dimensional time series data $[V(t), V(t+\tau), V(t+2\tau)]$ are generated by an application of a time delay τ which can, in principle, be chosen arbitrarily. Practical criterion for the choice of time delay is proposed by Fraser and Swinney.[40)]

Two-dimensional phase-space portraits for YIG are constructed as $V(t)$ vs $V(t+\tau)$ by taking $\tau=3\mu$sec, which is about one-fifth of the fundamental period. The results are shown in Fig. 10. At $P=1.66$ dB, the oscillations are regular and the phase portrait for period-2 is shown at $P=2.20$ dB. The amplitude of the oscillations increases with increasing driving power. Phase portraits from $P=2.73$ dB to $P=3.60$ dB show chaos. At $P=4.08$ dB, period-halving transition from chaos to period-4, to period-2 at $P=4.32$ dB, and to period-1 at $P=5.25$ dB occurs. The regular oscillations go to the chaotic state at much higher driving power after a periodic window.

If the system is periodic the trajectory forms a closed orbit. A set of phase-space trajectories for all possible initial conditions in a chaotic system is called a strange attractor when two nearby trajectories exponentially part from one another with time. The exponential separation of trajectories causes stretching to form a sheet-like attractor which contracts perpendicular to the direction of stretching. But since the attractor lies within a bounded region of phase space, the attractor must also exhibit folding. In order to examine the three-dimensional character of the strange attractor in parallel-pumped magnon systems, we have generated three-dimensional data from the original single time series data by a procedure of time delay. Figure 11 is the view of the two-dimensional projection of a strange attractor on a $V(t)$ vs

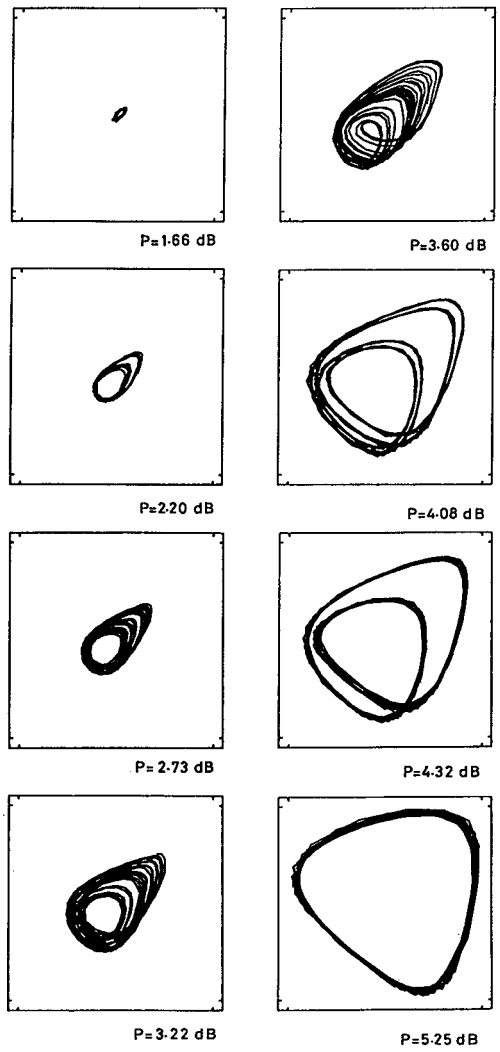

Fig. 10. Phase-space portrait $V(t)$ vs $V(t+\tau)$ of YIG.[31]

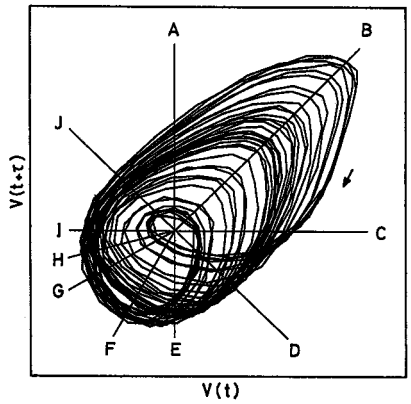

Fig. 11. Two-dimensional projection of the strange attractor of YIG at $P=3.60$ dB.[27),31)]

$V(t+\tau)$ plane. The vertical axis to the plane is the $V(t+2\tau)$ axis. Figure 12 presents the Poincaré sections constructed by the intersection of positively directed trajectories with the plane, which is normal to the page passing through the (A-J) of Fig. 11. As is clearly seen in this figure, the trajectories form a two-dimensional sheet. By examining the evolution of the trajectories in the Poincaré sections at successive points along the strange attractor, the sequence of stretching (H→I→J→A→B) and folding (C→D→E→F→G→H) is evidently observed. Since an infinitely repeated stretching and folding process with the evolution of trajectories gives a fractal structure to the strange attractor, the fractal dimension is one of the character-

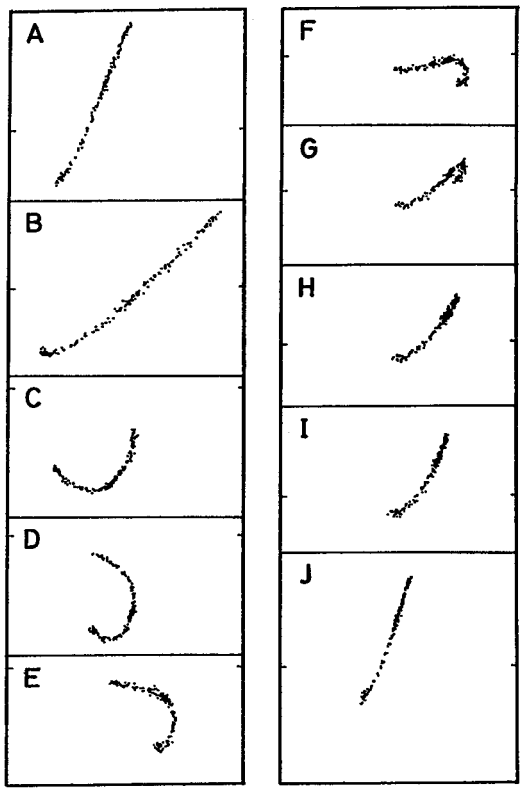

Fig. 12. Poincaré sections of the strange attractor on the plane normal to the paper passing through (A-J) lines of Fig. 11.[27),31)]

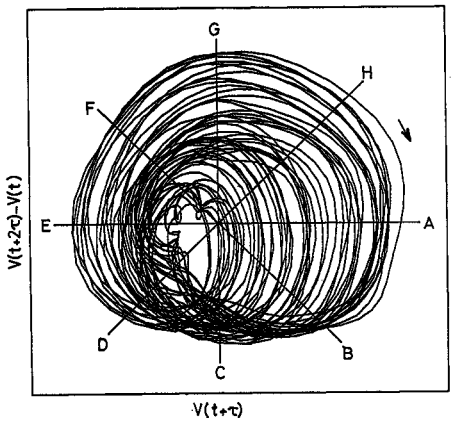

Fig. 13. Two-dimensional projection of the strange attractor of MACC.[30),31)]

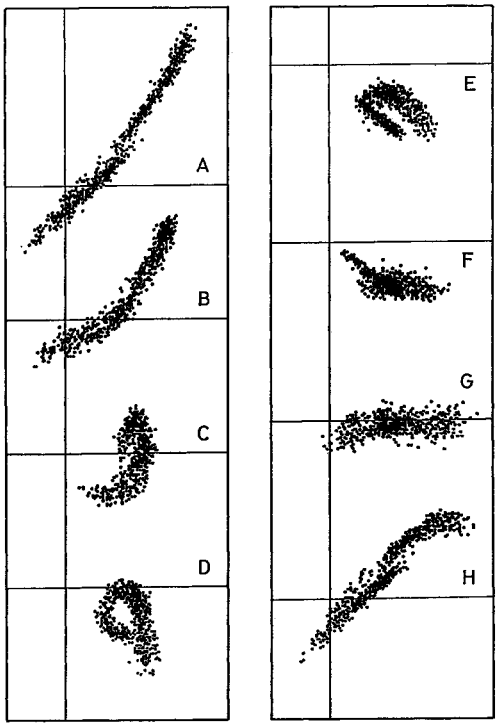

Fig. 14. Poincaré sections of the strange attractor of the plane normal to the paper passing through (A-H) lines of Fig. 13.[30),31)]

istic measures of chaos.

Strange attractors of chaos of parallel-pumped magnons in another ferromagnet MACC are also investigated. By taking the time delay $\tau=1.75\times10^{-5}$ sec, which is nearly one-eighth of the fundamental period, three-dimensional time series data, $V(t)$, $V(t+\tau)$, and $V(t+2\tau)$ are generated from the time series data. Figure 13 is the best view of the two-dimensional projection of the strange attractor on the (101) plane, $V(t+2\tau)-V(t+\tau)$ vs $V(t+\tau)$. The third axis, which is normal to the page, is $V(t+2\tau)+V(t)$. Figure 14 presents the Poincaré sections constructed by the intersection of positively directed trajectories with the plane, which is normal to the page passing through lines A-H in Fig. 13. Figure 14(A) is the Poincaré section which shows the most stretched sheet of trajectories although the trajectories are rather scattered compared with those of YIG. By examining the evolution of trajectories in the Poincaré sections at successive points along the strange attractor, the sequence of folding (B→C→D→E) and stretching (F→G→H→A) can be observed.

4.5. *Fractal dimension of strange attractors*

As mentioned in the preceding section, a strange attractor is not a simple sheet, but a sheet formed by infinitely repeated stretching and folding process by time evolution. One of the characteristic measures of a strange attractor is its fractal dimension, which allows one to distinguish between deterministic chaos and random noise. For example, the dimension of a fixed point in the phase space is zero and that of a limit cycle is one, while that of white noise is infinite. By the standard definition of dimension, for example the Hausdorff dimension,[39)] a strange attractor generally has a noninteger dimension.

Grassberger and Procaccia[41)] have developed a simple procedure to derive a

fractal dimension from experimental data. Their procedure is as follows: Consider a set of N points, (V_i, $i=1, 2, \cdots, N$), on an attractor embedded in a phase space of n dimensions. Since the phase space is n-dimensional, each point V_i is composed of n-data, $V(t)$, $V(t+\tau)$, $\cdots$, $V(t+(n-1)\tau)$ with a fixed time increment between successive measurements. The spatial correlation of the attractor is defined by

$$C(r)=\frac{1}{N^2}\sum_{i,j=1}^{N}\theta(r-|\boldsymbol{V}_i-\boldsymbol{V}_j|)\,, \tag{29}$$

where $\theta(x)=0$ if $x<0$ and $\theta(x)=1$ if $x>0$. The correlation integral, $C(r)$, counts the number of pairs whose distance $|\boldsymbol{V}_i-\boldsymbol{V}_j|$ is smaller than a given r. Their idea is that $C(r)$ grows for small r like a power law,

$$C(r)\sim r^d\,. \tag{30}$$

If all data points are on a line, $C(r)$ is proportional to r. If these are on a surface, $C(r)$ should be proportional to r^2. Therefore the dimension d of the attractor is given by the slope of $\ln C(r)$ versus $\ln r$ in a certain range of r. Since the dimension of experimental random noise is usually larger than that of the attractor, the slope of $\ln C(r)$ for noise is large below a certain r which is determined by the strength of noise.[42]

Figure 15 shows the correlation integral $C(r)$ as a function of r with logarithmic scale for the experimental data of YIG whose strange attractor is shown in Fig. 11. By using experimental time series data with time increment $\tau=2$ μsec, a set of N points in n-dimensional phase space is constructed as follows:

$$V_i=V(i\tau), V((i+1)\tau), \cdots, V((i+n-1)\tau), \qquad i=1, 2, \cdots, N\,. \tag{31}$$

Here n is the dimension of phase space wherein the attractor is embedded and is called the embedding dimension. To construct n-dimensional points we have used a time delay τ which is the same as the time increment τ of the time series data. Figure

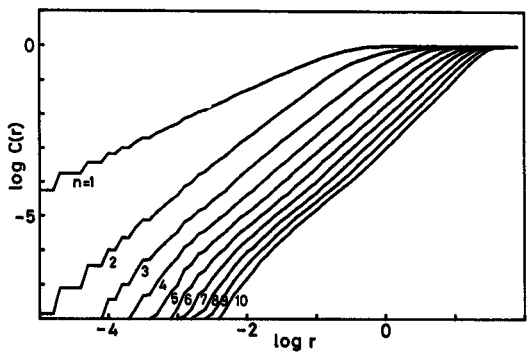

Fig. 15. Correlation integral $\ln C(r)$ in YIG as a function of distance r with embedding dimensions of $n=1$ to 10.[27),31)]

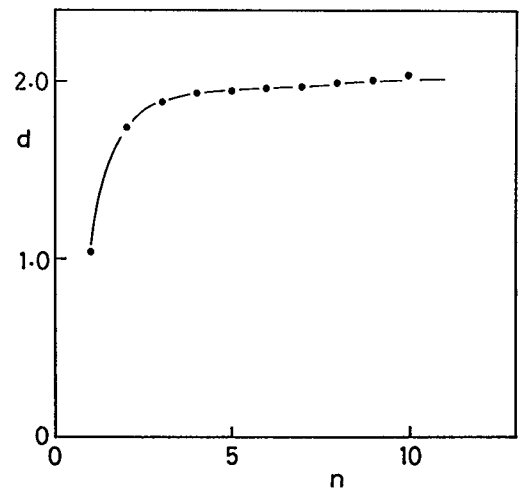

Fig. 16. Correlation exponent d in YIG as a function of embedding dimension n.[31)]

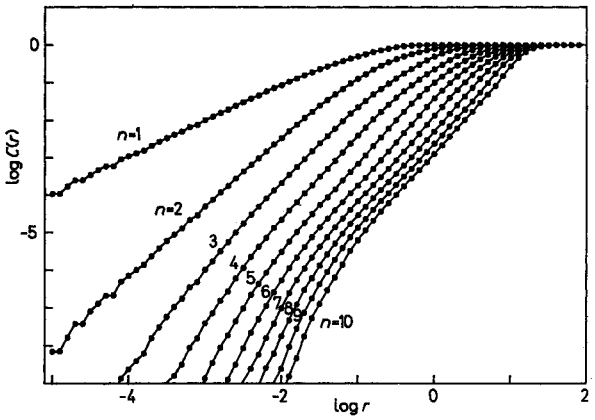

Fig. 17. Correlation integral $\ln C(r)$ in MACC as a function of distance r with embedding dimensions of $n=1$ to 10.[30]

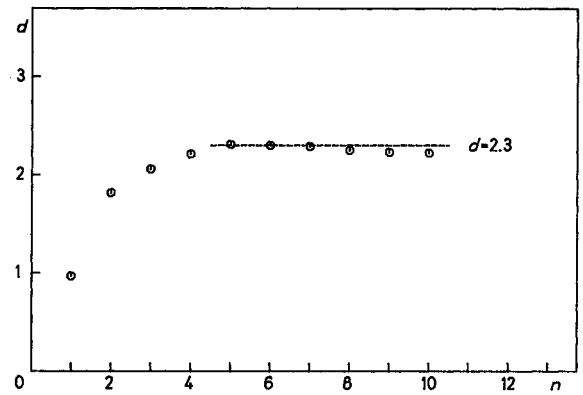

Fig. 18. Correlation exponent d in MACC as a function of embedding dimension n.[30]

15 shows $\ln C(r)$ as a function of $\ln r$ for embedding dimensions from $n=1$ to 10. The correlation exponent d is estimated from the portion of the curves in the range $-4<\ln C(r)<-2$, where the curves are almost straight and should give characteristics of the fractal structure. The correlation exponents d obtained in this way are shown in Fig. 16 as a function of the embedding dimension n. With increasing n, d increases and becomes nearly constant, $d=2.0$, which is the fractal dimension of the strange attractor in YIG. The error to the fractal dimension comes from slope variation within the scaling range of $\ln C(r)$.

The same procedure has been applied to MACC whose correlation integral $\ln C(r)$ are shown in Fig. 17 as a function of $\ln r$. As is seen in this figure, $\ln C(r)$ in the region below -5 has a larger slope which is especially noticeable for larger embedding dimensions. This may arise from experimental noise and fluctuations. The correlation exponent d determined in the range of $-4<\ln C(r)<-2$ are shown in Fig. 18 as a function of the embedding dimension n. With increasing n, d increases and becomes nearly constant, $d=2.3\pm0.2$. This procedure has been applied to the analysis of the data obtained at other driving power P. The fractal dimension increases from $d=1.6\pm0.4$ up to $d=3.4\pm0.3$.

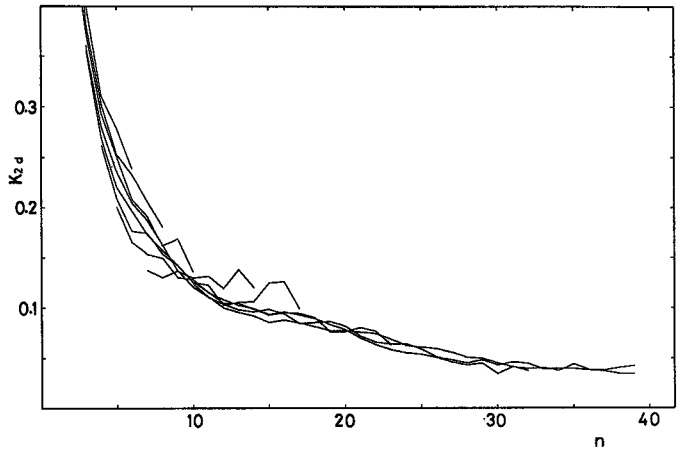

Fig. 19. Values of $\ln[C_n(r)/C_{n+1}(r)]$ as a function of embedding dimension n in YIG.[31] The extrapolated value to $n=\infty$ gives K_2 entropy as $K_2=0.03$.

The correlation integral, $C(r)$, is useful to estimate the Kolmogorov entropy K which gives a degree of chaos. A regular trajectory has $K=0$, while random noise has $K=\infty$. A deterministic chaotic system has a finite K which is equal to the sum of the positive Lyapunov exponents.[39),43),44)] A brief explanation of Lyapunov exponents will be given later.

A method to derive a K_2 entropy from the correlation integral $C(r)$ has been given by Grassberger and Procaccia[45] as follows:

$$K_2=\lim_{r\to 0}\lim_{n\to\infty}\ln\left[\frac{C_n(r)}{C_{n+1}(r)}\right]\leq K\,. \tag{32}$$

Since K_2 is a lower bound to the Kolmogorov entropy K, $K_2>0$ provides a sufficient condition for chaos.

In order to estimate the K_2 entropy from the time series data of YIG, the quantity $\ln[C_n(r)/C_{n+1}(r)]$ was calculated up to the embedding dimension $n=39$. The results are shown in Fig. 19 as a function of n. The extrapolated value of K_2 to $n=\infty$ is 0.03. This result indicates that the Kolmogorov entropy K is positive. The K_2 entropy for MACC is also positive and is 0.06.

4.6. *Lyapunov exponents*

Another quantitative measure of a strange attractor is positive Lyapunov exponents which characterize the average rate of exponential divergence of nearby trajectories within the attractor. The magnitude of the positive exponents is a measure of the degree of chaos. Negative Lyapunov exponents characterize the average rate of exponential convergence of trajectories onto the attractor. The largest Lyapunov exponent, λ, can be conventionally computed from a one-dimensional return map as follows:[46]

$$\lambda=\frac{1}{n}\sum_{i=1}^{n}\ln|f'(V_i)|\,, \tag{33}$$

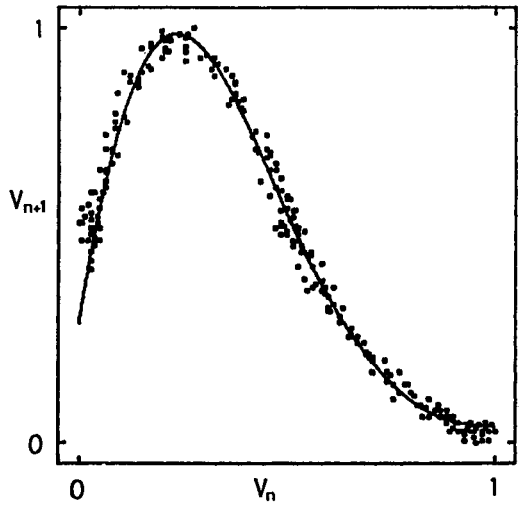

Fig. 20. Return map of YIG.[27),31)]

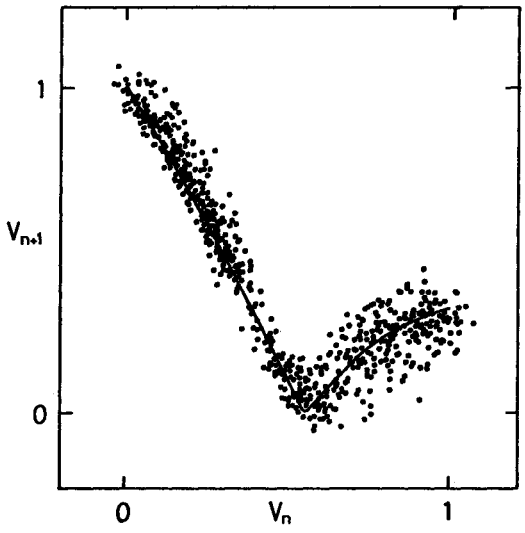

Fig. 21. Return map of MACC.[30)]

where $f'(V_i)$ is the derivative of the map at V_i.

In order to construct a return map from the experimental time series data, the intensity of the $(n+1)$-th peak, V_{n+1}, is plotted as a function of n-th peak, V_n. As shown in Fig. 20, the data fall on a single-hump curve which is similar to other chaotic systems, for example the Belousov-Zhabotinskii reaction.[47] This result indicates that the system is deterministic. The solid line shown in the figure is the eleventh order polynomial function obtained by the least squares method. By applying this function to Eq. (33) with $n=5\times10^4$ iterations, the largest Lyapunov exponent is obtained as $\lambda=0.34$. A positive Lyapunov exponent indicates sensitive dependence on initial conditions and also measures the average loss of information after one iteration. Therefore, the magnitude of the positive exponent is a measure of the degree of chaos.

Since the strange attractor of MACC has a more complicated structure than that of YIG, the map constructed from the $(n+1)$-th peak of the experimental time series data as a function of the n-th peak does not come together on a simple curve. The best one, which is shown in Fig. 21 is constructed as follows; the $(\bar{1}01)$ plane, $[V(t+2\tau)+V(t)$ vs $V(t+\tau)]$ of the three-dimensional phase space is taken as a Poincaré section. The intersection of positively directed trajectories of the strange attractor with this plane is examined. A one-dimensional return map, Fig. 21, is constructed by plotting the value of the $(n+1)$-th point on the Poincaré section as a function of the preceding value, V_n. Since these data are scattered, probably by experimental fluctuations, two cubic curves connected at the middle point are found by fitting the data by the least square method. By using this empirical map with $n=5\times10^4$ iterations, the largest Lyapunov exponent is obtained as $\lambda=0.21$, which is smaller than that of YIG.

§ 5. Experimental observation of chaos under perpendicular pumping

Bryant, Jeffries and Nakamura[20] studied auto-oscillations accompanied with the first-order perpendicular pumped instability in a YIG sphere, at frequency 9.2 GHz and at room temperature. They found rich behavior including single-mode excitation; low-frequency collective oscillations when two modes are excited; quasiperiodicity, locking, and chaos when three modes are excited; and abrupt hysteretic onset of wide-band chaos at the Suhl threshold. They have experimentally observed two kinds of route to chaos; cascade of period-doubling bifurcations and quasiperiodicity. Figure 22 shows the regions and boundaries of oscillations behavior. Their theoretical model is in principle identical to that employed in § 3.

As the field H_0 is slowly increased at constant pump power, a series of sharp dips, which is independent of time, is observed as shown in Fig. 23, with a spacing $\Delta H_0 = 0.156$ G. This can be understood as high-order spatial resonance modes within the sphere as first found by Jantz and Schneider.[48] However, as H_0 is increased to a field where simultaneous excitation of two modes is possible due to overlap, the signal shows a low frequency auto-oscillations by nonlinear mode-mode coupling. These periodic collective oscillations display successive period doubling and become chaos. As the magnetic field is further increased, second oscillations whose frequency, f_2, is incommensurate with the first one, f_1, start. The power spectra show peaks at the combination frequencies $f_{nm} = nf_1 + mf_2$, with n, m integers. These quasiperiodic oscillations are attributed to the excitation of three spin-wave modes.

Gibson and Jeffries[18] observed low frequency auto-oscillations in perpendicular-pumping second-order Suhl instability experiment is gallium-doped YIG at 1.3 GHz. These oscillations display period-doubling bifurcation route to chaos and periodic

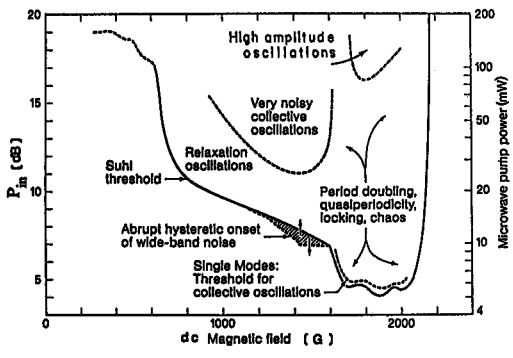

Fig. 22. Regions and boundaries of the first-order Suhl instability and oscillations in YIG measured by Bryant et al.[20]

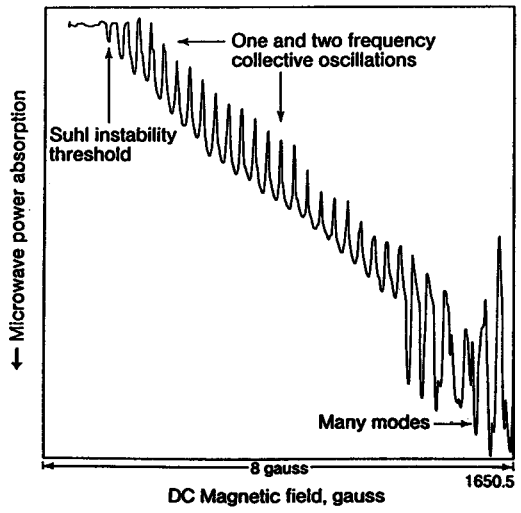

Fig. 23. Microwave absorption in YIG as the magnetic field is increased through the Suhl threshold, showing sequence of single spatial spin-wave modes, spaced by $\Delta H_0 = 0.157$ G.[20]

window as the driving field is increased above the threshold for the Suhl instability. Theoretical simulation of nonlinear four-magnon interaction Hamiltonian was performed by Rezende et al.[16] and Zhang and Suhl.[15]

§ 6. Concluding remarks

Characteristics of chaos in spin-wave instabilities under intense microwave pumping are summarized in this review. A theoretical model of chaos due to a nonlinear four-magnon interaction under parallel pumping has been given. Numerical solutions display a rich variety of periodic and chaotic trajectories. A multifractal structure, singularity spectrum $f(\alpha)$, is numerically studied for two modes model which includes a microwave cavity mode. Experimental results observed in two ferromagnets, YIG and MACC, show strange attractors with fractal structure which has been confirmed by an infinitely repeated stretching and folding process with the evolution of trajectories in the phase space. Several parameters, that is to say, fractal dimension, Lyapunov exponent and Kolmogorov entropy, which characterize the strange attractors have been derived from the experimental time-series data. Experimental observation on chaos under perpendicular pumping has also discussed.

An interest in chaos in spin-wave instabilities is still growing. Theoretical investigations have been recently developed by Lim and Huber[49] and Gill and Zachary.[50] Singularity spectra $f(\alpha)$ of the strange attractor in YIG are experimentally obtained and compared with numerical simulations by the present authors and Nakamura.[51] The singularity spectra are considered to be excellent characterizations of strange attractors.

References

1) R. W. Damon, Rev. Mod. Phys. **25** (1953), 239.
2) N. Bloembergen and S. Wang, Phys. Rev. **93** (1954), 72.
3) H. Suhl, J. Phys. Chem. Solids **1** (1957), 209.
4) E. S. Schlömann, J. J. Green and U. Milano, J. Appl. Phys. **31** (1960), 386S.
5) F. R. Morgenthaler, J. Appl. Phys. **31** (1960), 95S.
6) T. S. Hartwick, E. R. Peressini and M. T. Weiss, J. Appl. Phys. **32** (1961), 223S.
7) V. V. Zautkin, V. S. L'vov and S. S. Starobinets, Sov. Phys.-JETP **36** (1973), 96.
8) V. V. Zautkin and S. S. Starobinets, Sov. Phys.-Solid State **16** (1974), 446.
9) V. L. Grankin, V. S. L'vov, V. I. Motorin and S. L. Musher, Sov. Phys.-JETP **54** (1981), 405.
10) V. E. Zakharov, V. S. L'vov and S. S. Starobinets, Sov. Phys.-JETP **32** (1971), 656.
11) V. E. Zakharov, V. S. L'vov and S. S. Starobinets, Sov. Phys.-Usp. **17** (1975), 896.
12) K. Nakamura, S. Ohta and K. Kawasaki, J. of Phys. **C15** (1982), L143.
13) S. Ohta and K. Nakamura, J. of Phys. **C16** (1983), L605.
14) M. J. Feigenbaum, J. Stat. Phys. **19** (1978), 25.
15) X. Y. Zhang and H. Suhl, Phys. Rev. **A32** (1985), 2530.
16) S. M. Rezende, O. F. de Alcantara Bonfim and F. M. de Aguiar, Phys. Rev. **B33** (1986), 5153.
17) H. Yamazaki, J. Phys. Soc. Jpn. **53** (1984), 1155.
18) G. Gibson and C. Jeffries, Phys. Rev. **A29** (1984), 811.
19) P. Bryant, C. Jeffries and K. Nakamura, Phys. Rev. Lett. **60** (1988), 1185.
20) P. Bryant, C. Jeffries and K. Nakamura, Phys. Rev. **A38** (1988), 4223.
21) P. Bryant, C. Jeffries and K. Nakamura, J. Appl. Phys. **64** (1988), 5382.
22) P. Bryant, C. Jeffries and K. Nakamura, Nucl. Phys. **B2** (1987), 25.

23) T. L. Carroll, L. M. Pecora and F. J. Rachford, J. Appl. Phys. **64** (1988), 5396.
24) H. Benner, F. Rodelsperger, H. Seitz and G. Wiese, J. de Phys. **49** (1988), C8-1603.
25) S. M. Rezende, F. M. de Aguiar and O. F. de Alcantara Bonfim, J. Magn. Magn. Mater. **54-57** (1986), 1127.
26) F. M. de Aguiar and S. M. Rezende, Phys. Rev. Lett. **56** (1986), 1070.
F. M. de Aguiar, A. Azevedo and S. M. Rezende, Phys. Rev. **B39** (1989), 9448.
27) M. Mino and H. Yamazaki, J. Phys. Soc. Jpn. **55** (1986), 4168.
28) H. Yamazaki, D. R. Barberis and F. Waldner, *Proc. 22nd Congr. AMPERE on Magnetic Resonance and Related Phenomena,* ed. K. A. Müller et al. (University of Zurich, 1984), p. 123.
29) H. Yamazaki and M. Warden, J. Phys. Soc. Jpn. **55** (1986), 4477.
30) H. Yamazaki, M. Mino, H. Nagashima and M. Warden, J. Phys. Soc. Jpn. **56** (1987), 742.
31) H. Yamazaki, J. Appl. Phys. **64** (1988), 5391.
32) A. I. Smirnov, Sov. Phys.-JETP **63** (1986), 222; **67** (1988), 969.
33) F. Waldner, D. R. Barberis and H. Yamazaki, Phys. Rev. **A31** (1985), 420.
34) F. Waldner, J. of Phys. **C21** (1988), 1243.
35) M. Warden and F. Waldner, J. Appl. Phys. **64** (1988), 5386.
36) A. Libchaber and A. Maurev, *Nonlinear Phenomena at Phase Transitions and Instabilities,* ed. T. Riste (Plenum, New York, 1982), p. 259.
37) K. Nakamura, M.Mino and H. Yamazaki, J. de Phys. **49** (1988), C8-1599.
38) T. C. Halsey, M. H. Jensen, L. P. Kadanoff, I. Procaccia and B. I. Shraiman, Phys. Rev. **A33** (1986), 1141.
39) J.-P. Eckmann and D. Ruelle, Rev. Mod. Phys. **57** (1985), 617.
40) A. M. Fraser and H. L. Swinney, Phys. Rev. **A33** (1986), 1134.
41) P. Grassberger and I. Procaccia, Physica **9D** (1983), 189.
42) A. B. Mizrachi, I. Procaccia and P. Grassberger, Phys. Rev. **A29** (1984), 975.
43) G. Benettin, L. Galgani and J. M. Strelcyn, Phys. Rev. **A14** (1976), 2338.
44) I. Shimada and T. Nagashima, Prog. Theor. Phys. **61** (1979), 1605.
45) P. Grassberger and I. Procaccia, Phys. Rev. **A28** (1983), 2591.
46) K. Tomita and T. Kai, J. Stat. Phys. **21** (1979), 65.
47) J.-C. Roux, R. H. Simoyi and H. L. Swinney, Physica **8D** (1983), 257.
48) W. Jantz and J. Schneider, Phys. Status Solidi **31** (1975), 595.
49) S. P. Lim and D. L. Huber, Phys. Rev. **B37** (1988), 5426.
50) T. L. Gill and W. W. Zachary, Phys. Lett. **A128** (1988), 419.
51) M. Mino, H. Yamazaki and K. Nakamura, Phys. Rev. **B**, to be published.